Numerical Heat Transfer, Part B, 43: 567–586, 2003

1040-7790/03 $12.00 + .00
DOI: 10.1080/10407790390122186

A KARHUNEN–LOÈVE-BASED APPROACH TO NUMERICAL SIMULATION OF TRANSITION IN RAYLEIGH–BÈNARD CONVECTION

Hakan I. Tarman
Department of Engineering Sciences, Middle East Technical University, Ankara, Turkey

A Karhunen–Loève (K–L) basis is generated empirically, using a database obtained by numerical integration of Boussinesq equations representing Rayleigh–Benard convection in a weakly turbulent state in a periodic convective box with free upper and lower surfaces. This basis is then used to reduce the governing partial differential equation (PDE) into a truncated system of amplitude equations under Galerkin projection. In the generation and implementation of the basis, the symmetries of the PDE and the geometry are fully exploited. The resulting amplitude equations are integrated numerically and it is shown that, with the use of the K–L basis in the present formulation, the known dynamics of the flow in the transition region is completely captured.

INTRODUCTION

The transition to chaos in the case of Rayleigh–Benard (R-B) thermal convection takes the form of discrete steps as the forcing parameter, Rayleigh number (Ra), is gradually increased. The first step after the conductive static state is the two-dimensional steady flow in the form of rolls as shown theoretically by Schlüter et al. [1]. When Ra is increased further, the fluid motions become time-dependent. The time dependence is shown theoretically by Busse [2] for a convection layer with stress-free boundaries and a low Prandtl number (Pr) fluid to be oscillatory in the form of traveling waves propagating along the axis of the rolls. It was shown that the motion in this oscillatory regime is associated with the generation of the vertical vorticity and hence is three-dimensional. Further increase in Ra causes appearance of chaotic time dependence preceded by quasi-periodic regime. Numerical studies by McLaughlin and Orszag [3] for rigid boundary conditions and by Curry et al. [4] at high Prandtl number with stress-free boundary conditions have shown that transition to chaotic regime follows a route consistent with the scenario of Ruelle et al. [5], namely, that the appearance of a third oscillatory mode in a nonlinearly coupled system likely leads to broad-band frequency excitations and chaos. Under various

Received 21 May 2002; accepted 9 January 2003.
The author is grateful to L. Sirovich for many fruitful discussions from which this work originated.
Address correspondence to Hakan I. Tarman, Department of Engineering Science, Middle East Technical University, Ankara 06531, Turkey. E-mail: tarman@metu.edu.tr

NOMENCLATURE

a	expansion coefficient	Pr_o	reference Prandtl number ($=0.72$)
A	aspect ratio ($=L/H$)	Q	coefficient of quadratic terms in the momentum equation
A_o	reference aspect ratio ($=2\sqrt{2}$)		
b	expansion coefficient for mechanical component	Q'	coefficient of quadratic terms in the thermal equation
B	coefficient of buoyancy terms in the momentum equation	r	normalized Rayleigh number ($=\mathrm{Ra}/\mathrm{Ra}_c$)
B'	coefficient of buoyancy terms in the thermal equation	r_t	normalized transition Rayleigh number ($=\mathrm{Ra}_t/\mathrm{Ra}_c$)
c	expansion coefficient for thermal component	Ra	Rayleigh number ($=g\beta H^4\alpha/\kappa\nu$)
		Ra_c	critical Rayleigh number ($=27\pi^4/4$)
D	coefficient of diffusive terms in the momentum equation	Ra_o	reference Rayleigh number ($=15\times\mathrm{Ra}_c$)
D'	coefficient of diffusive terms in the thermal equation	Ra_t	transition Rayleigh number
		$\mathbf{R}(\mathbf{x},\mathbf{x}')$	two-point correlation tensor
D_4	dihedral group	s	$=\pi/\sqrt{2}$
$\mathbf{e}_z$	unit vector antiparallel to the direction of gravity	t	time
		T	temperature
f	frequency	T_c	class of thermal K–L modes
H	vertical dimension	$\mathbf{u}$	velocity vector, (u,v,w)
$\mathbf{k}$	index vector, $(k_x\ k_y\ n)$	$\mathbf{U}$	mechanical K–L bases
$\mathbf{k}^*$	conjugate index vector, $(-k_x\ -k_y\ n)$	U_c	class of mechanical K–L modes
		$\mathbf{v}$	snapshots of realizations
ℓ	index representing $\{\mathbf{k}\ ,\mathbf{k}^*\}$ pair	$\mathbf{v}^\ell$	flowlet
L	horizontal dimension	$\mathbf{x}$	spatial coordinate, (x,y,z)
n	vertical quantum number	δ	Kronecker delta
(M,N)	truncation parameter pair	$\boldsymbol{\Theta}$	thermal K–L bases
Nu	Nusselt number	λ	K–L eigenvalue
p	pressure	$\boldsymbol{\Phi}$	vertical profile of K–L bases
Pr	Prandtl number ($=\nu/\kappa$)	$\boldsymbol{\Psi}$	K–L bases

fluid conditions and geometries, Gollub and Benson [6] experimentally found several other routes of transition to chaos including a phase-locked regime preceding the transition. Various explanations were suggested regarding the interpretation and the causal mechanisms of the oscillatory motions of R–B convection preceeding the chaotic regime. Willis and Deardorff [7] suggested that the oscillations could be explained by the theory developed by Howard [8], which is based on a periodic instability of the thermal boundary layer releasing thermals and yielding an $\mathrm{Ra}^{2/3}$ dependence of the frequency of oscillations. A different explanation associating the oscillations with circulating spots of relatively warm or cold fluid was invoked by Krishnamurti [9] through experimental observations. Later, Willis and Deardorff [10], based on their experimental observations, concluded that the thermal oscillations are caused by lateral displacements of the updrafts and downdrafts during oscillations of the wavy rolls.

Karhunen–Loève (K–L) basis is empirical in nature and is computed using K–L decomposition technique from an experimentally or numerically generated database representative of the underlying phenomena. Since the basis is specific to the phenomena under consideration, it provides an optimal parametrization of the database (data compression) and an optimal representation of the dynamics of the phenomena when used for a low-dimensional dynamical representation. Numerous prior studies have adopted the K–L procedure in a variety of low-dimensional dynamical studies [11–15]. In this work, Boussinesq equations (BE) are integrated numerically at the selected reference parameter values of $\mathrm{Ra}_o = 15 \times \mathrm{Ra}_c$, where Ra_c is the critical Rayleigh number at which convective motion first sets in, $\mathrm{Pr}_o = 0.72$, and the aspect ratio, $A_o = 2\sqrt{2}$, with horizontally periodic and vertically stress-free boundary conditions. The resulting numerical database is used to generate the K–L basis, which, in turn, is used to reduce the BE to a system of amplitude equations through a Galerkin procedure. In the present formulation unlike previous treatments [16–18], the K–L decomposition technique is applied separately to the mechanical and thermal components of the numerical solution field, resulting in two orthonormal K–L basis sets, and the mean field is not subtracted off prior to the computation of the basis, thus removing the need to include the mean field separately in the amplitude equations [19]. In the computation of the K–L basis, the symmetries arising from the BE and the geometry of the spatial domain are fully exploited, leading to a database enlargement and sharper basis elements. It is observed that the K–L basis elements each carry a physical character of the underlying flow and that they gather in distinct symmetry classes which provide the grounds for a rational truncation scheme. The truncated amplitude equations are then integrated numerically in time for a range of Ra covering the transition regime. It is shown that the known dynamics of the flow in the transition regime are completely captured by these relatively low-dimensional model amplitude equations and, further, the seemingly disparate results in the literature are shown to be embodied in the solution of these model equations. Thus, we conclude that the present K–L formulation leads to a more robust formulation which is better suited to a parametric study.

We now elaborate further on the essential way in which the present formulation differs from the previous treatments involving low-dimensional modeling. The Boussinesq equations specify the nature of the coupling mechanical and thermal effects, but the quantitative degree of this is unknown until the solution is determined. This quantification is an important factor in a K–L decomposition which hopes to couple the two forms of energy. (See [16] for a discussion of this point.) In this article we avoid this issue by utilizing separate K–L decompositions for mechanical and thermal effects. Although this increases the dimension of the description, it leads to the robust formulation.

Next, there is no attempt to extract the mean field from the dynamics. Specifically, the mean temperature field is given by

$$\frac{\partial}{\partial z}\langle wT\rangle = \frac{\partial^2\langle T\rangle}{\partial z^2} \tag{1}$$

(see below for notation). In view of the dynamical nature of a calculation, the implicit (infinite) time average, indicated by brackets, is replaced by an average over space. For practical reasons spatial domains in a simulation cannot be extensive enough for stationarity to be achieved [13]. For example, in simulations of channel flow, the bulk flow exhibits time variation, which if the computational domain were to become unbounded would disappear. In the present instance of low-dimensional modeling, the lack of time stationarity is exacerbated by the fact that Eq. (1) is projected onto a lower-dimensional manifold. This in fact leads to relatively rapid time variations in violation of the assumption of stationarity [13]. In many instances this has led to an inconsistent formulation in which quantities taken to be time-stationary turn out to be quite the opposite. This is avoided in the present treatment by the simple device of not subtracting off the mean.

This leads to the third departure from standard practice. In the cited references the practice has been to introduce mean quantities into the equations. As Eq. (1) illustrates a mean quantity is proportional to the product of two fluctuating quantities. Further, mean quantities appear in the equations of motion multiplied by a fluctuating quantity. Thus, evolution equations contain cubic terms, although the Navier–Stokes equations are manifestly quadratic. It then follows that the dynamical equations which result in the present formulation have quadratic and not cubic direction fields.

RAYLEIGH–BENARD FLOW

Rayleigh–Benard thermal convection problem is the instability of a Boussinesq fluid layer on an infinite horizontal plane heated from below and cooled from above in the presence of gravity and is governed by the Boussinesq equations,

$$\nabla \cdot \mathbf{u} = 0 \tag{2a}$$

$$\frac{\partial \mathbf{u}}{\partial t} + \mathbf{u} \cdot \nabla \mathbf{u} = -\nabla p + \mathrm{Ra}\,\mathrm{Pr}\,T\mathbf{e}_z + \mathrm{Pr}\,\Delta \mathbf{u} \tag{2b}$$

$$\frac{\partial T}{\partial t} + \mathbf{u} \cdot \nabla T = w + \Delta T \tag{2c}$$

All quantities have been made dimensionless by the standard normalization [20], e.g., the box height, H, is used to normalize $\mathrm{x} = (x, y, z)$. The two dimensionless parameters are Prandtl number, Pr, and Rayleigh number, Ra. The flow takes place in a box of dimensions $L \times L \times H$. The boundary conditions are imposed as the stress-free flow conditions

$$w = T = \frac{\partial u}{\partial z} = \frac{\partial v}{\partial z} = 0 \qquad \text{at } z = 0, 1 \tag{2d}$$

in the vertical and periodic in the horizontal x and y variables.

The database generated earlier [17] was obtained by numerically integrating Eqs. (2) using a Fourier-collocation spectral method [21] on a $20 \times 20 \times 20$ grid at $\mathrm{Pr}_o = 0.72$, $\mathrm{Ra}_o = 15 \times \mathrm{Ra}_c$, and $A_o = 2\sqrt{2}$. The aspect ratio corresponds to the wavelength of maximum linear instability [20].

DYNAMICAL APPROXIMATION

K–L Decomposition

A K–L basis [22–24] can be generated from an ensemble of snapshots of realizations $\mathbf{v}(\boldsymbol{x}, t)$. The elements of the basis set are the eigenfunctions of the integral equation,

$$\int_\Omega \mathrm{R}(\mathrm{x}, \mathrm{x}')\, \Psi^{\mathrm{k}}(\mathrm{x}')\, dx' = \lambda_{\boldsymbol{k}} \Psi^{\mathrm{k}}(\mathrm{x}) \tag{3}$$

the kernel of which is the two-point correlation tensor $R_{ij}(\mathbf{x}, \mathrm{x}') = \langle \mathrm{v}_i(\boldsymbol{x}, t)\, \mathrm{v}_j(x', t) \rangle$. The angle brackets denote ensemble average. If the process is statistically stationary, ergodicity permits replacement of the ensemble average by an average over time. In our case three indices are required to specify a basis set in three spatial dimensions. **k** represents these indices (see below).

The existence of orthonormal eigenfunctions spanning the space follows from the symmetry of R_{ij}. An element of the space can be expressed in the form of a modal decomposition

$$\mathbf{v}(\boldsymbol{x}, t) = \sum_{\mathbf{k}} a_{\mathbf{k}}(t)\, \Psi^{\mathrm{k}}(\boldsymbol{x}) \tag{4}$$

and the expansion coefficients

$$a_{\mathbf{k}} = \left(\Psi^{\mathrm{k}}, \mathbf{v}\right) \equiv \int_{\Omega} \sum_{i} \mathrm{v}_i(\boldsymbol{x}, t) \left[\Psi_i^{\mathbf{k}}(x)\right]^* dx \tag{5}$$

are statistically orthogonal,

$$\left\langle a_{\mathbf{k}}(t)\, a_{\mathbf{l}}^*(t) \right\rangle = \lambda_{\mathbf{k}}\, \delta_{\mathbf{kl}} \tag{6}$$

where * stands for complex conjugation. For **v** representing the flow, each eigenvalue, $\lambda_{\boldsymbol{k}}$, represents the mean energy of the flow projected on the direction $\boldsymbol{\Psi}^{\boldsymbol{k}}$ in the function space.

Symmetries

The consideration of the symmetries of the governing partial differential equation (PDE) ([23], part 2) is significant in the later approximation of the PDE by a K–L-based truncated system of ordinary differential equations (ODEs), see also [25]. Since each element of the group of symmetries produces an admissible solution, the ergodicity permits the introduction of the symmetries through the ensemble average in the generation of the K–L eigensolutions. The governing system of equations, Eqs. (2), is invariant under a discrete symmetry group in the form of reflectional and rotational symmetries in the horizontal and reflectional symmetry in the vertical mid-plane as well as a continuous symmetry group in the form of translational invariance in the horizontal directions [26].

Homogeneity in the horizontal directions leads to the translational invariance,

$$\mathrm{R}_{ij}(\mathbf{x}, \mathrm{x}') \equiv \mathrm{R}_{ij}(\boldsymbol{x} - x', y - y', z, z') \tag{7}$$

which in turn implies that the eigenfunctions are in the form

$$\begin{aligned} \Psi^{\mathrm{k}}(\mathrm{x}) \equiv \Psi(k_x, k_y, n; \mathrm{x}) &= \Phi^{\mathrm{k}}(z) \exp(i k_x s x)\ \exp(i k_y s y) \\ &= \sum_{k_z} \widehat{\Phi}^{\mathbf{k}}(k_z) \exp(\pi i k_z z) \exp(i k_x s x) \exp(i k_y s y) \end{aligned} \tag{8}$$

where $\mathbf{k} = (k_x\ k_y\ n)$ is the index vector, $k_x s$ and $k_y s$ are wave numbers, and n is the vertical quantum number. Due to the reflectional and rotational symmetries, the eigensolutions come with a maximum 8-fold degeneracy, i.e.,

$$\lambda_{(\pm k_x\ \pm k_y\ n)} = \lambda_{(\pm k_x\ \mp k_y\ n)} = \lambda_{(\pm k_y\ \pm k_x\ n)} = \lambda_{(\pm k_y\ \mp k_x\ n)} \tag{9}$$

(Since the planform is a square, the reflectional and rotational symmetries in the horizontal plane form the dihedral group D_4 containing eight elements.) The reflectional symmetry in the vertical mid-plane $z = \frac{1}{2}$ renders the individual functions either odd or even in $z = \frac{1}{2}$, which implies that the summation in Eq. (8) is over only odd or only even integers k_z, respectively.

These lead to a more convenient representation of the flow in terms of *flowlets*, $\mathbf{v}^\ell$,

$$\mathbf{v}(\boldsymbol{x}, t) = \sum_\ell \mathbf{v}^\ell = \sum_{\mathbf{k}} \{a_k(t)\Psi^{\mathbf{k}}(x) + a_{\mathbf{k}^*}(t)\, \Psi^{\mathbf{k}^*}(\boldsymbol{x})\} \tag{10}$$

Each flowlet is a real incompressible flow satisfying the boundary conditions. The summation index ℓ runs through the conjugate pairs of the K–L modes $\{\mathbf{k}\ ,\ \mathbf{k}^*\}$ such that $\Psi^{\mathbf{k}^*} = \left(\Psi^{\mathbf{k}}\right)^*$ and $a_{\mathbf{k}^*} = a^*_{\mathbf{k}}$.

K–L Representation

We use this formalism to create two ensembles, containing separately the mechanical $\mathbf{u}$ and thermal components T of the flow. The two orthonormal K–L basis sets are denoted by $\mathbf{U}^{\mathbf{k}}$ and $\Theta^{\mathbf{k}}$, so that the mechanical motion is represented by,

$$\mathbf{u}(x, t) = \sum_\ell \mathbf{u}^\ell = \sum_k \left\{ b_{\mathbf{k}}(t)\, \mathbf{U}^k(\boldsymbol{x}) + b_{\mathbf{k}^*}(t)\, \mathbf{U}^{\mathbf{k}^*}(x) \right\} \tag{11}$$

and thermal component by

$$T(\boldsymbol{x}, t) = \sum_\ell T^\ell = \sum_{\mathbf{k}} \left\{ c_{\mathbf{k}}(t)\, \Theta^{\mathbf{k}}(\boldsymbol{x}) + c_{\mathbf{k}^*}(t)\, \Theta^{\mathbf{k}^*}(\boldsymbol{x}) \right\} \tag{12}$$

where $b_{\mathbf{k}}$ and $c_{\mathbf{k}}$ are individually statistically orthogonal [Eq. (6)].

The eigenvalues corresponding to the K–L decomposition of the mechanical and thermal components for the first ten K–L modes are shown in Table 1. For the reasons presented in the introduction, the mean temperature is not subtracted from the thermal field, thus the energy content of the thermal K–L mode [0, 0, 1], whose vertical profile is the most similar to that of the mean temperature, is substantial and is close in value to the mean. Note that K–L modes belonging to the same degenerate family are grouped together, however they are ordered based on the individual eigenvalues rather than the total energy content of each degenerate family. The justification is that in the absence of the degeneracy, the K–L modes would appear individually and the corresponding eigenvalues would be an appropriate measure of the energy content. Figure 1 shows the flowlets $\mathbf{u}^\ell$ and T^ℓ of Eqs. (11) and (12) associated with some of the K–L modes. They are the building blocks of the mechanical and thermal components of the total flow, and as basis functions they are very specific to the underlying phenomena.

Galerkin Projection

Next, Galerkin projection is applied to the Boussinesq equations. To accomplish this, we introduce the truncated K–L representations,

Table 1. Normalized K–L eigenvalues for the first 10 degenerate mechanical and thermal modes[a]

	Mechanical K–L modes				Thermal K–L modes			
Index	**k**	Normalized eigenvalue	Degeneracy	Percent cumulative energy	**k**	Normalized eigenvalue	Degeneracy	Percent cumulative energy
1	[0 1 1]	1.0000	4	51.39	[0 0 1]	1.0000	1	53.86
2	[1 1 1]	0.2639	4	64.95	[0 1 1]	0.1272	4	81.27
3	[0 1 2]	0.1654	4	73.45	[1 1 1]	0.0320	4	88.17
4	[0 0 1]	0.0637	2	75.09	[0 2 1]	0.0048	4	89.19
5	[1 2 1]	0.0435	8	79.57	[1 2 1]	0.0042	8	91.00
6	[0 2 1]	0.0379	4	81.52	[0 2 2]	0.0042	4	91.89
7	[1 1 2]	0.0338	4	83.26	[0 1 2]	0.0037	4	92.70
8	[1 1 3]	0.0181	4	84.19	[0 0 2]	0.0036	1	92.90
9	[0 3 1]	0.0179	4	85.11	[0 3 1]	0.0033	4	93.61
10	[1 2 2]	0.0167	8	86.83	[0 1 3]	0.0025	4	94.15

[a]The degeneracy implies for example that [0 1 1] stands for the degenerate family [(0 1 1), (0 − 1 1), (1 0 1), (−1 0 1)] as defined by Eq. (9).

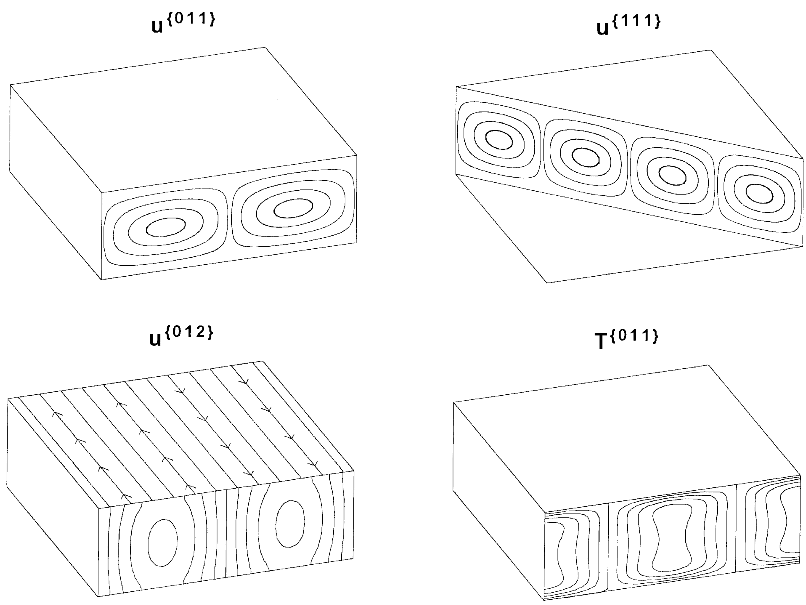

Figure 1. The flows associated with some of the K–L modes. The streamline pattern for the flows $\mathbf{u}^{\{0\ 1\ 1\}}$ and $\mathbf{u}^{\{1\ 1\ 1\}}$ show two-dimensional roll motion along the x axis and the diagonal, respectively. The flow associated with $\mathbf{u}^{\{0\ 1\ 2\}}$ is pumping motion in and out of the y–z plane as shown by a combined picture of streamlines and isovelocity contours of the x component of velocity. This flow is characterized by having nonzero vertical vorticity component. The flow associated with the thermal mode $T^{\{0\ 1\ 1\}}$ is compatible with the roll motion as shown by its isothermal contours.

$$\mathbf{u}(\boldsymbol{x}, t) \approx \sum_{\ell \in U_c} \mathbf{u}^\ell \qquad \text{and} \qquad T(\boldsymbol{x}, t) \approx \sum_{\ell \in T_c} T^\ell \tag{13}$$

where each summation is over a suitable class of flowlets, denoted by U_c and T_c. In choosing these classes we respect the symmetries carried by the degeneracies shown in Eq. (9).

Under projection, the resulting amplitude equations have the form

$$\frac{db_{\mathbf{k}}}{dt} = \mathrm{Ra}\ \mathrm{Pr}\, B_{\mathbf{kp}}\, c_{\mathbf{p}} + \mathrm{Pr}\, D_{\mathbf{kp}} b_{\mathbf{p}} + Q_{\mathbf{kpq}}\, b_{\mathbf{p}}\, b_{\mathbf{q}} \tag{14}$$

$$\frac{dc_{\mathbf{k}}}{dt} = B'_{\mathbf{kp}}\, b_{\mathbf{p}} + D'_{\mathbf{kp}}\, c_{\mathbf{p}} + Q'_{\mathbf{kpq}}\, b_{\mathbf{p}}\, c_{\mathbf{q}} \tag{15}$$

with the summation convention over repeated indices, and only over the sets U_c and T_c. The coefficients are defined for $\mathbf{p} = \{p_x\ p_y\ n_p\}$, $\mathbf{q} = \{q_x\ q_y\ n_q\}$, and $\mathbf{k} = \{k_x\ k_y\ n_k\}$ as follows:

$$B_{\mathbf{kp}} = \left(\mathbf{U}^{\mathbf{k}}\,,\ T^{\mathbf{p}}\,\mathbf{e}_z\right) \qquad \text{and} \qquad D_{\mathbf{kp}} = \left(\mathbf{U}^{\mathbf{k}}\,,\ \Delta\mathbf{u}^{\mathbf{p}}\right) \tag{16}$$

$$B'_{\mathbf{kp}} = \left(\Theta^{\mathbf{k}}\,,\ w^{\mathbf{p}}\right) \qquad \text{and} \qquad D'_{\mathbf{kp}} = \left(\Theta^{\mathbf{k}}\,,\ \Delta T^{\mathbf{p}}\right) \tag{17}$$

with $p_x = k_x$ and $p_y = k_y$,

$$Q_{\mathbf{kpq}} = -\frac{1}{2}\left(\mathbf{U}^{\mathbf{k}}\,,\ \mathbf{u}^{\mathbf{p}}\cdot\nabla\mathbf{u}^{\mathbf{q}} + \mathbf{u}^{\mathbf{q}}\cdot\nabla\mathbf{u}^{\mathbf{p}}\right) \qquad \text{and} \qquad Q'_{\mathbf{kpq}} = -\left(\Theta^{\mathbf{k}}\,,\ \mathbf{u}^{\mathbf{p}}\cdot\nabla T^{\mathbf{q}}\right) \tag{18}$$

with $p_x + q_x = k_x$, $p_y + q_y = k_y$ [19]. Observe that quadratic cross-coupling appears only in the thermal equation [Eq. (15)], where it is the only nonlinearity.

TRUNCATION SCHEME

In implementing the Galerkin procedure we do not endeavor to minimize the order of the resulting dynamical system. Although our approach is based on the choice of the most energetic modes, we will also include modes which carry the full complement of symmetries that accompany the energetic modes. To illustrate this point, according to Table 1 the most energetic space dependent thermal mode is (0 1 1). As seen in Figure 2E, this mode is an even function in z. Figure 2F shows (0 1 2), which is the odd counterpart of (0 1 1). Although the former is not as important as the latter from the point of view of energy, we carry it along with (0 1 1) in order to explore the full symmetries of this grouping. As will be seen, this desire to always carry a full complement of symmetries will lead to relatively low energy modes tagging along. This becomes more apparent in the case of the velocity modes.

The most energetic mechanical mode is (0 1 1) and is shown in Figure 2A, as is (0 1 2) in Figure 2B. It is clear that these two are unrelated. In fact, as is clear from Figure 2C, (0 1 3) is the odd counterpart of (0 1 2), while (0 1 4) in Figure 2D is the parity counterpart of (0 1 1). On a more analytical note we observe that (0 1 2) and (0 1 3) carry vertical vorticity, with (0 1 2) having nonzero mean component independent of the vertical coordinate z. (They are also referred to as parasitic, since they do not involve convective heat transport.) On the other hand, (0 1 1) and (0 1 4) have zero vertical vorticity. We regard the four such modes as carrying the full

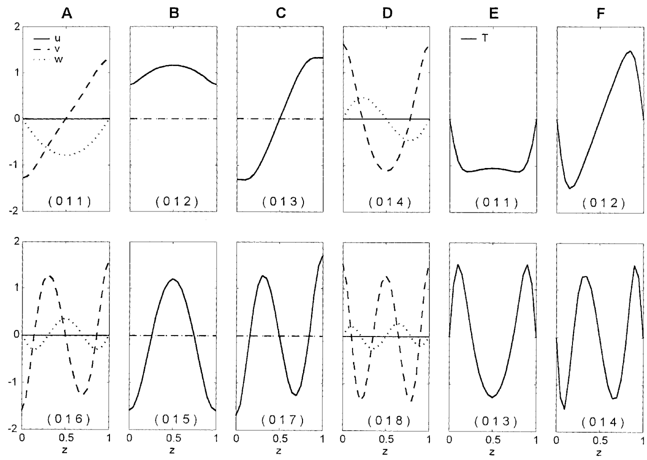

Figure 2. The vertical profiles of the mechanical and thermal K–L eigenfunctions for the family of modes (0 1 n). This is a typical plot indicating the two cycles [$N = 2$, see Eq. (19)] of the grouping of the symmetries labeled by A, B, C, and D for the mechanical modes and by E and F for the thermal modes.

complement or a cycle of physical symmetries. We observe that (0 1 4) has relative energy 0.62%, which illustrates our remark about low energy modes tagging along. It should be noted that the splitting of mechanical modes into those with and without vertical vorticity occurs naturally in the K–L decomposition and agrees with the practice adopted in stability theory ([2]) and is discussed in more detail in [27].

Furthermore, an inspection of Table 1 indicates that most energy is captured by the low wave numbers. In particular, at $r = 15$ roughly 90% of the energy is captured by the modes, $\mathbf{k}$, satisfying $\sqrt{k_x^2 + k_y^2} \leq 3$. Based on these observations, we will truncate to include modes which satisfy

$$\left\{ [k_x, k_y, n] \mid \sqrt{k_x^2 + k_y^2} \leq M \text{ and } 1 \leq n \leq c \cdot N \right\} \tag{19}$$

where $c = 4$ for mechanical and 2 for thermal modes, respectively. N denotes the number of symmetry cycles. The integer parameter pair (M, N) will be used to specify the truncation in our simulations.

RESULTS

We have performed numerical experiments by integrating the truncated amplitude equations for some selected truncation parameter pairs (M, N) near the onset of the convective motion at $r = 1$. The numerical integration is performed starting from the initial conditions set as zero for the amplitudes of the mechanical modes and small random numbers for those of the thermal modes for these runs. In Table 2, the resulting flow for the selected truncations of (3, 2) and (3, 3) is compared with the asymptotic solution of Schlüter [1]. Note that the flow quantities compare better for (3, 3) in comparison to those for (3, 2) at $r = 1.005$ and $r = 1.01$. The poor performance of truncation (3, 2) is due to built-in vertical resolution of the K–L basis elements being too high for this low r values. In case of

Table 2. Comparison of maximum velocity and maximum temperature given by the asymptotic solution of Schlüter et al. [1] and the numerical solution at truncation parameter pairs (3, 2) and (3, 3)[a]

		$r = 1.005$		$r = 1.01$		$r = 1.1$	
		$v_{\max}$	$T_{\max}$	$v_{\max}$	$T_{\max}$	$v_{\max}$	$T_{\max}$
Asymptotic solution		1.088	0.0517	1.539	0.0728	4.867	0.211
Numerical solution	(3, 2)	0	0	0.662	0.0300	4.794	0.184
	(3, 3)	1.087	0.0501	1.544	0.0700	4.882	0.186

[a]At $r = 1.1$, the comparison is intended between the two truncation parameter pairs since the asymptotic solution may not be valid at this r. The zero values signify no motion.

truncation $(3,\ 3)$, this problem is alleviated by supply of more degrees of freedom for the flow to adjust the vertical resolution to the low resolution requirement at low r. As the value of N in the truncation parameter pair (M, N) is increased, more K–L basis elements are introduced into the flow simulation in a manner of increased vertical complexity. The comparable values of the flow quantities between $(3,\ 2)$ and $(3,\ 3)$ at $r = 1.1$ in Table 2 shows that the relatively higher vertical resolution requirement as r increases is met by the use of $(3,\ 2)$. Further, numerical experiments to determine the intervals in which lie the critical r values for transition to the periodic and the quasi-periodic stages of the flow are performed for various truncation parameter pair values. A satisfactory qualitative agreement is observed among the selected truncations as shown in Table 3. These considerations support the selection of the truncation parameter pair $(3,\ 2)$ for the subsequent qualitative study of the transition. The reduced computational labor also plays a role in this selection which involves the inclusion of $120 + 60$ (mechanical + thermal) conjugate pairs of K–L modes. The partial list (for $N = 1$ only) of K–L modes involved in the simulation is shown in Table 4. As initial conditions for the subsequent runs with increasing r, randomly perturbed amplitudes of the thermal field computed for the preceding r values are used.

The K–L power spectrum plot at $r = 1.9$ in Figure 3 shows that the two-dimensional roll solutions are dominant as shown by the physical manifestation of this spectrum in Figure 4. The alignment of the rolls is in the y direction which evolved from randomly selected initial conditions. The K–L modes excited in this steady-state regime have the common parity that $k_x + k_z$ is even. As r is increased from 1.9 to 2.0, transition to a periodic state is observed numerically. The

Table 3. Intervals for critical r values in which numerically observed transition to the indicated states occur for some selected truncation parameter pairs (M, N)

	Interval for critical r	
(M, N)	Periodic state	Quasi-periodic state
(3, 2)	(1.9, 2.0)	(2.9, 3.0)
(3, 3)	(1.8, 1.9)	(2.7, 2.8)
(4, 2)	(2.0, 2.1)	(2.7, 2.8)
(5, 2)	(1.9, 2.0)	(2.8, 2.9)

Table 4. K–L modes included for the selected truncation parameter pair (3, 2)[a]

A		B		C		D		E		F	
ℓ	$\{k_x\ k_y\ n\}$	ℓ	$\{k_x\ k_y\ n\}$	ℓ	$\{k_x\ k_y\ n\}$	ℓ	$\{k_x\ k_y\ n\}$	ℓ	$\{k_x\ k_y\ n\}$	ℓ	$\{k_x\ k_y\ n\}$
1	{0 1 1}	3	{0 1 2}	5	{0 1 3}	7	{0 1 4}	61	{0 1 1}	63	{0 1 2}
2	{1 0 1}	4	{1 0 2}	6	{1 0 3}	8	{1 0 4}	62	{1 0 1}	64	{1 0 2}
9	{1 1 1}	11	{1 1 2}	13	{1 1 3}	15	{1 1 4}	65	{1 1 1}	67	{1 1 2}
10	{1 −1 1}	12	{1 −1 2}	14	{1 −1 3}	16	{1 −1 4}	66	{1 −1 1}	68	{1 −1 2}
17	{1 2 1}	21	{1 2 2}	25	{1 2 4}	29	{1 2 3}	69	{1 2 1}	73	{1 2 2}
18	{1 −2 1}	22	{1 −2 2}	26	{1 −2 4}	30	{1 −2 3}	70	{1 −2 1}	74	{1 −2 2}
19	{2 1 1}	23	{2 1 2}	27	{2 1 4}	31	{2 1 3}	71	{2 1 1}	75	{2 1 2}
20	{2 −1 1}	24	{2 −1 2}	28	{2 −1 4}	32	{2 −1 3}	72	{2 −1 1}	76	{2 −1 2}
33	{0 2 1}	35	{0 2 2}	37	{0 2 4}	39	{0 2 3}	77	{0 2 2}	79	{0 2 1}
34	{2 0 1}	36	{2 0 2}	38	{2 0 4}	40	{2 0 3}	78	{0 2 2}	80	{2 0 1}
41	{0 3 1}	43	{0 3 2}	45	{0 3 4}	47	{0 3 3}	81	{0 3 1}	83	{0 3 2}
42	{3 0 1}	44	{3 0 2}	46	{3 0 4}	48	{3 0 3}	82	{3 0 1}	84	{3 0 2}
49	{2 2 1}	51	{2 2 2}	53	{2 2 3}	55	{2 2 4}	85	{2 2 1}	87	{2 2 2}
50	{2 −2 1}	52	{2 −2 2}	54	{2 −2 3}	56	{2 −2 4}	86	{2 −2 1}	88	{2 −2 2}
57	{0 0 1}					59	{0 0 3}	89	{0 0 2}	90	{0 0 1}
58	{0 0 2}					60	{0 0 4}				

[a]For brevity, only those modes for $N = 1$ are listed. The modes, under the symmetry grouping labels A, B, C, D for mechanical and E, F for thermal, carry the common symmetry characteristics mentioned in the text. The index ℓ is used in the identification of the modes in the K–L power spectrum plots (Figure 3) and is arbitrary otherwise. The curly brackets represent the conjugate pair; for example, { 1 2 1} stands for {(1 2 1), (-1 -2 1)}. The {0 0 n} modes appear in conjugate-pair notation for simplicity; they are, of course, singletons.

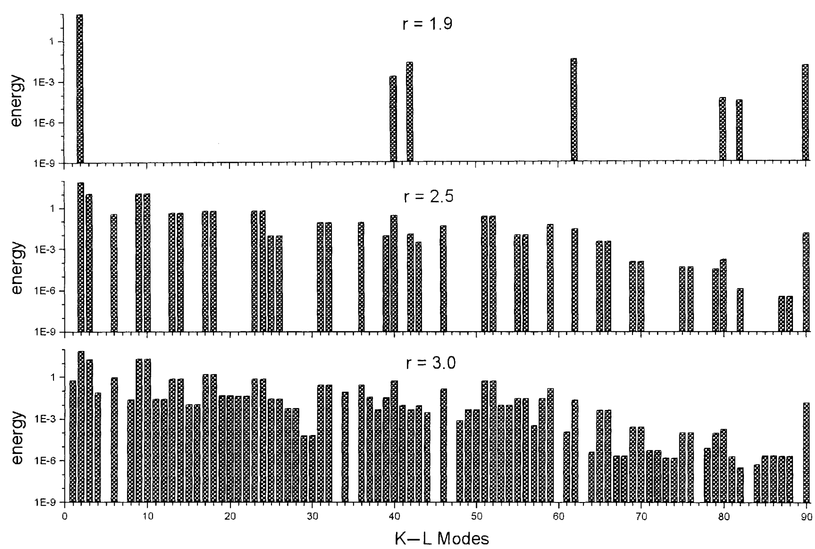

Figure 3. The magnitudes (averaged in time) of the complex expansion coefficients of the K–L modes excited at the indicated r values. The indexing of the modes is based on Table 4.

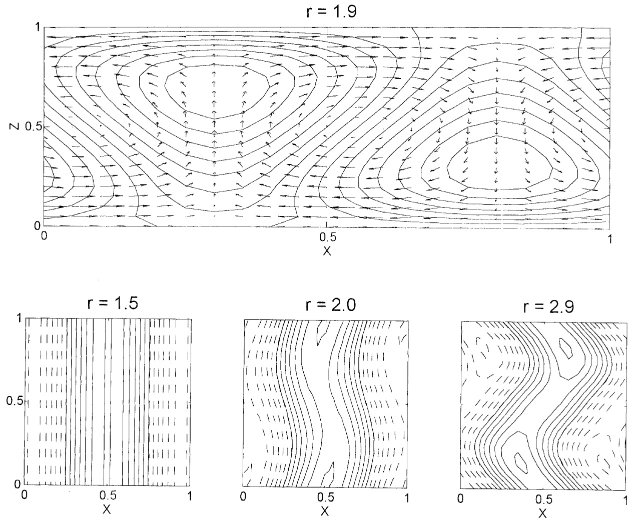

Figure 4. The two-dimensional roll motion with the corresponding temperature distribution in the x–z plane in the steady-state regime at $r = 1.9$, and typical contour plots of the vertical velocity in the horizontal mid-plane at $r = 1.5$, 2.0, 2.9 at a particular time. Here, x and y coordinates are individually normalized; in fact, $0 \leq x, y \leq 2\sqrt{2}$.

appearance of the fundamental oscillation frequency $f_1 = 2.165$ is shown in Figure 5 at $r = 2.9$. All the newly excited modes as shown in the K–L power spectrum plot in Figure 3 at $r = 2.5$ in the periodic state still have the common parity that $k_x + k_z$ is even. The functional dependence of u, v, w, T of these newly excited K–L modes on the horizontal variable y and time t are of the form $\cos[k_y(sy + 2\pi f_1 t)]$ or $\sin[k_y(sy + 2\pi f_1 t)]$, where the time dependence enters through the phase of the complex K–L expansion coefficients while their magnitudes are constant in time. This indicates periodic translation of the modes in the y direction which is parallel to the roll axis. An example of this is provided by the observation that the amplitudes of those conjugate pairs of K–L modes with ($k_x \neq 0$ and $k_y \neq 0$) appear in pairs having equal magnitudes in the K–L power spectrum plot at $r = 2.5$ in Figure 3. It is also observed that the phases of the amplitudes of these modes are related in a special way, as shown in Figure 6 for two typical cases for the mechanical K–L modes ($\{1\ 1\ 1\}$ and $\{1\ -1\ 1\}$) and ($\{1\ 2\ 1\}$ and $\{1\ -2\ 1\}$). These indicate that the wave patterns associated with the modes ($\{k_x\ k_y\ n\}$ and $\{k_x\ -k_y\ n\}$) combine to produce the effect of traveling wave along the y axis. Since the modes that formed the two-dimensional roll solution in the steady-state regime still have no time dependence in this periodic state, the motion manifests itself as traveling waves superimposed onto the rolls as shown by the sequence of contour plots of the vertical velocity in the horizontal mid-plane in Figure 4 for $r = 1.5$, 2.0, 2.9. After the appearance of the traveling waves at the critical r value in the interval (1.9, 2.0), the wave pattern gradually becomes sharper-crested, which was also observed by Lipps [28] in his numerical simulation. The most energetic mode that contributes to the generation of vertical vorticity in the periodic state is the mode $\{0\ 1\ 2\}$, which has nonzero mean component independent of the vertical coordinate z. This is consistent with the linear

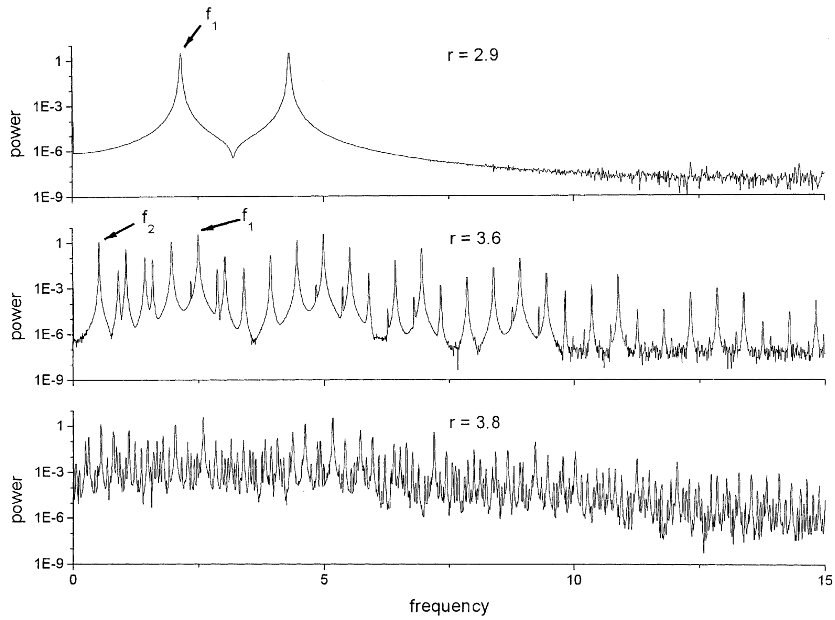

Figure 5. The frequency spectrum corresponding to the time series generated by sampling the vertical velocity component w at a particular spatial location. These are typical in the periodic, doubly periodic, and at the start of the nonperiodic regimes.

stability analysis of Busse [2], who reported the z-independent component of the vertical vorticity as a cause of the oscillatory behavior.

Transition to a doubly periodic (quasi-periodic) state is observed numerically as r is increased from 2.9 to 3.0. This is shown later by a segment of typical time signal in this state at $r = 3.6$ in Figure 8. The appearance of the second incommensurate frequency $f_2 = 0.529$ at $r = 3.6$ is shown in Figure 5. The newly excited modes, in this regime at $r = 3.0$, as shown in the K–L power spectrum plot in Figure 3, have the common parity that $k_x + k_z$ is odd, which breaks the spectral even parity of the previous regime. The two primary frequencies f_1 and f_2 are shown to

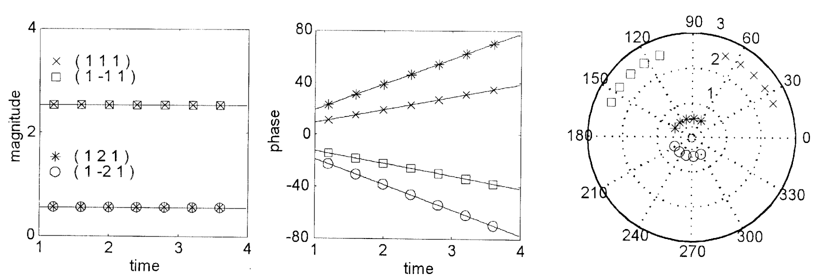

Figure 6. The time evolution of the magnitudes, the phases, and the polar representation of the complex K–L amplitudes at $r = 2.5$ in the periodic state for the mechanical K–L modes ({1 1 1}and{1 − 1 1}) and ({1 2 1} and {1 − 2 1}). The slopes of the phases are given by $\pm 2\pi k_y f_1$ and the phases are related by phase(1 − 1 1) = π − phase(1 1 1) and by phase(1 − 2 1) = −phase(1 2 1).

increase monotonically with r in Figure 7. The frequency of the traveling waves can be seen to increase monotonically with r in [29]. The evolution of the ratio f_1/f_2 with r as shown in Figure 7 appears to be in a weakly frequency-locked state as the ratio takes values between 4.67 and 4.73 at selected points in a range of r from 3.0 to 3.7. As the ratio starts to decrease at $r = 3.8$, the frequency spectrum develops a marked change toward nonperiodicity as shown in Figure 5. This transition seems to agree with *route-I* transition scenario, as it is termed in [6], based on experimental observations. Our observation that the transition to the quasi-periodic and then to the nonperiodic state coincides with the appearance of the modes with opposite spectral parity may be consistent with the observation in [3] that implicates the symmetry-breaking modes with the onset of chaos.

As mentioned above, the physical manifestation of the periodic motion is in the form of waves traveling along the axis of otherwise two-dimensional steady rolls, and this motion evolves with the frequency of oscillations, f_1. Next, we attempt to identify the physical picture of motion in the quasi-periodic regime by using a simple sampling technique which helps isolate the motions evolving with the second frequency of oscillations, f_2 ($f_2 < f_1$). For this purpose, a typical time signal in this regime at $r = 3.6$ is sampled at a rate of $1/f_1$ as marked by $1, 2, 3, \ldots$ in Figure 8 to obtain a time series. Clearly, the variation in this time series is associated with the frequency f_2. The corresponding evolution of motion is shown in the same figure by the isothermal contours in a specified region of a y–z slice in the convective box. These series of frames are ordered with respect to the time series. The physical picture clearly shows thermals periodically being released from the lower thermal boundary layer (similar releases are observed to occur from the upper thermal boundary layer at a different y–z slice). This is in line with Howard's theory [8] on the periodic instability of the thermal boundary layer, as mentioned in the introduction. Further, the computed dependence of the frequency of oscillations is found to follow very closely Howard's prediction of $r^{2/3}$ as shown in Figure 7. When totality of the motion is considered, these thermals would experience lateral displacements. This might be the physical picture of oscillations described in [10] based on their experimental observations, as mentioned in the introduction.

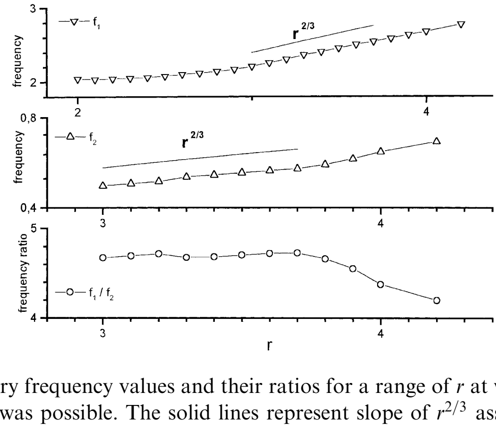

Figure 7. The two primary frequency values and their ratios for a range of r at which the identification of the primary frequencies was possible. The solid lines represent slope of $r^{2/3}$ associated with the periodic instability of the thermal boundary layer due to Howard [8].

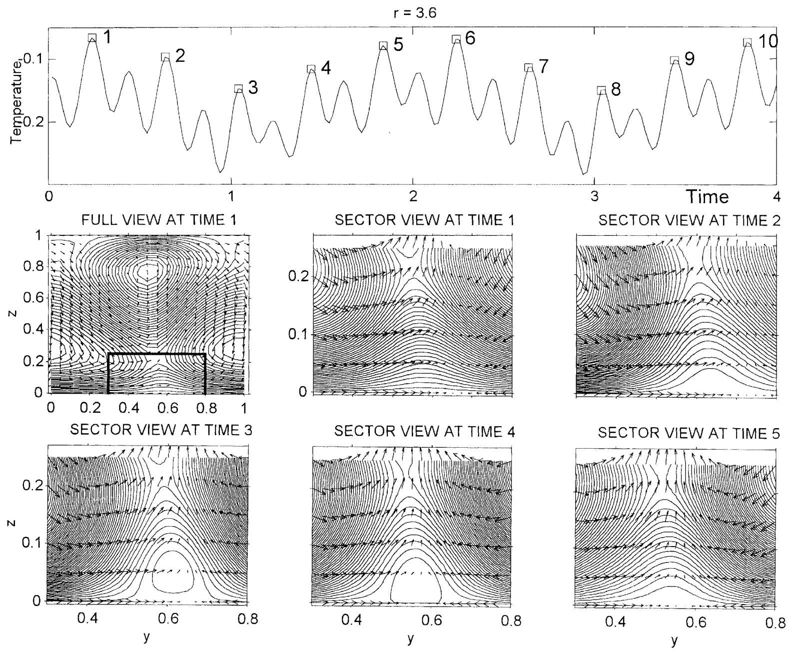

Figure 8. The evolution of the flow in a specified sector of the yz slice in the convective box. The frames of isothermal contours show a cycle of release of thermals from the lower boundary layer. Each frame is numbered in accordance with the time series marked on the signal depicting variation of temperature at a spatial location at $r = 3.6$. The marked points on the signal are sampled at a rate of $1/f_1$ to generate a $1/f_2$ periodic time series ($f_1 > f_2$).

In order to clarify the nature of the apparent transition from doubly periodic to nonperiodic (chaotic) regime, we have performed a numerical experiment by introducing oscillation in the form

$$r(t) = r(0)[1 + \epsilon \sin(2\pi f t)] \tag{20}$$

at $r \equiv r(0) = 3.4$ in the middle of the frequency-locked regime (see Figure 7). We choose $\epsilon = 0.1$ and the oscillation frequency $f = 1.0$ to be incommensurate with and between the frequencies of the quasi-periodic regime at $r = 3.4$ which are $f_1 = 2.401$ and $f_2 = 0.513$. The comparison of the power spectrum plots at $r = 3.4$ in Figure 9 shows that the introduction of the third incommensurate frequency produces early broad-band spectral excitations. This is similar to the behavior observed in transition from quasi-periodic state at $r = 3.6$ to nonperiodic state at $r = 3.8$. Furthermore, the two frequencies at $r = 3.4$ in its natural evolution are now replaced by $f_1 = 2.384$ and $f_2 = 0.521$ with the ratio $f_1/f_2 = 4.58$ which has dropped from $f_1/f_2 = 4.68$ in its natural evolution. This drop in the ratio was also observed in Figure 7 as the nonperiodic regime sets in. These observations might explain the transition to the nonperiodic regime as a result of the appearance of a naturally occurring incommensurate third frequency, which breaks the frequency-locked regime and suggests that the transition to nonperiodic regime occurs as predicted by Ruelle [5] and observed by McLaughlin and Orszag [3] and Curry [4] as mentioned in the introduction.

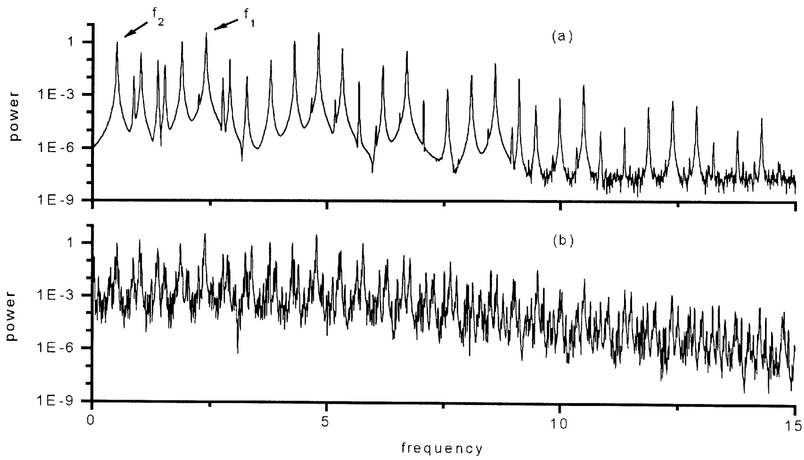

Figure 9. The frequency spectrum at $r = 3.4$ corresponding to the time series generated by sampling the vertical velocity component w at a particular spatial location corresponding to (*a*) the natural quasi-periodic state and (*b*) the state after the oscillations in the form of Eq. (20) are introduced. The spectrum in (*b*) exhibits broad-band spectral excitation and noise induced by the introduction of the incommensurate third frequency to the quasi-periodic state in (*a*).

It is of interest to follow the change in Nusselt number (Nu) with r. The computed Nu values are marked by the up-triangle symbols in Figure 10. We have used higher truncation parameter values, namely (4, 2), in computation of these values due to the known sensitive dependence of Nu on the truncation as well as to relatively smaller number of runs needed in the computation of Nu compared to the earlier frequency spectrum computations. The transitions to the periodic and quasi-periodic regimes appear as kinks in Figure 10. The change of slope is emphasized by the solid lines representing the best fit where they intersect at $r = 1.99$ and $r = 2.69$. These satisfactorily compare with the critical r values in Table 3 for (4, 2). The manifestation of the transition as kinks in the dependence of Nu on r was observed

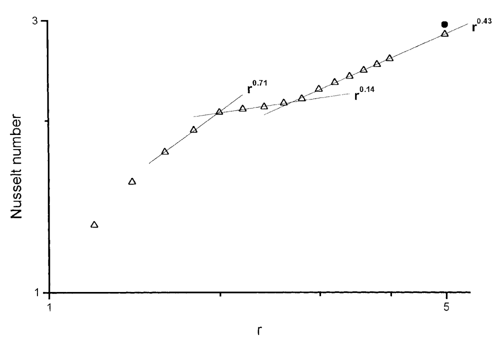

Figure 10. Nusselt number as a function of r; the solid circle marks the value from the numerical simulation by Deane and Sirovich [30] and the up-triangle symbols mark the values from the current K–L-based numerical simulation with the truncation parameter pair selected as (4, 2). The solid lines with the indicated dependence on r represent the best fit and are included to emphasize the change of slope.

experimentally by Krishnamurti [9]. The emergence of the parasitic modes as r is increased, such as the energetic mechanical K–L mode $\{0\ 1\ 2\}$ in the transition to periodic regime and $\{1\ 0\ 2\}$ in the transition to quasi-periodic regime, plays an important role in the appearance of the kinks, as they draw off energy from the active heat transfer modes without contributing to the generation of convective heat flux $\langle wT \rangle$. Clever and Busse [29] point out that the onset of traveling waves decreases the efficiency of the convective heat transport. This can be seen in Figure 10 by the decrease in the slope of the curve after the appearance of the first kink at the transition to periodic regime. The efficiency of the convective heat transport seems to be restored somewhat by the increase in the slope of the curve after the appearance of the second kink at the transition to quasi-periodic regime as more modes get excited in this regime. The comparison with the numerical simulation values of Deane and Sirovich [30] as shown by the solid circle at $r = 5.0$ shows satisfactory agreement.

DISCUSSION

The key step in the success of reproducing onset and the transition sequence of bifurcation behaviors using a truncated system is the mode selection. In the numerical simulations using K–L basis, the usual strategy has been to base the mode selection solely on the energy content of the modes, given conveniently by the corresponding eigenvalues. This in fact follows from the nature of the K–L decomposition, which extremizes the modal energy. However, modal energy content alone does not constitute a sufficient criterion to determine those modes that are not dynamically significant. This is even more so when the K–L basis is used for a range of off-reference control parameter values at which the basis is no longer optimal. In this work, the physical significance attached to the K–L modes together with the symmetry considerations add new rationale into the mode selection procedure and determine the success of the approach. Furthermore, the separate treatment of the mechanical and the thermal parts and the incorporation of the mean into the basis functions provide the K–L basis with the necessary freedom to adapt to the changing conditions in different regimes and enable efficient modeling of the dynamics of the system over a large range of the Rayleigh number.

An important advantage of the K–L basis over other general basis functions, such as Fourier or Chebyshev, is its empirical nature. This results in a compact representation of the dynamics in terms of the K–L basis. In this work, our objective has not been to determine a minimal dynamical system but rather to make all possible varieties of symmetries in a pool of $120 + 60$ conjugate K–L modes available to the dynamics. In fact, in the steady and periodic-state regimes, the excited few number of the modes provide a representation for the underlying dynamics (see Figure 3). Further analysis of the resulting dynamical system may bring down the necessary number of modes for a satisfactory qualitative representation of the dynamics in each regime. For example, the dominant excited modes, in the regime as the convective motion just sets in, form the flow as

$$\begin{aligned} \mathbf{u} &\approx b_1 \mathbf{U}^{(011)} + b_2 \mathbf{U}^{(101)} + \text{conjugate modes} \\ T &\approx c_0\, \Theta^{(001)} + c_1\, \Theta^{(011)} + c_2\, \Theta^{(101)} + \text{conjugate modes} \end{aligned} \quad . \tag{21}$$

corresponding to the case of the truncation parameter pair (3, 1). The dynamics of the complex coefficients b_n, c_n is governed by the coupled system of amplitude equations

$$\begin{aligned} \dot{b}_1 &= \mathrm{Ra}\ \mathrm{Pr}\ B_1 c_1 + \mathrm{Pr}\ D_1 b_1 \qquad & \dot{c}_1 &= B_1 b_1 + D_3 c_1 - Q_1 b_1 c_0 \\ \dot{b}_2 &= \mathrm{Ra}\ \mathrm{Pr}\ B_1 c_2 + \mathrm{Pr}\ D_1 b_2 \qquad & \dot{c}_2 &= B_1 b_2 + D_3 c_2 - Q_1 b_2 c_0 \\ \dot{c}_0 &= D_2 c_0 + Q_1 [b_1 c_1^* + b_1^* c_1 + b_2 c_2^* + b_2^* c_2] \end{aligned} \tag{22}$$

in which the coefficients are $B_1 = 0.5548$ for the buoyancy terms; $D_1 = -15.37$, $D_2 = -48.01$, $D_3 = -23.58$ for the diffusive terms; and $Q_1 = 1.89$ for the quadratic terms. The steady-state solution to Eq. (22) is found to be

$$\begin{aligned} b_1^2 + b_2^2 &= \left(\frac{\mathrm{Ra}\ B_1}{D_1}\right)^2 (c_1^2 + c_2^2) = \frac{D_2}{2 D_1 Q_1^2} (\mathrm{Ra} - \mathrm{Ra}_t) B_1^2 \\ c_0 &= \left(\frac{B_1}{Q_1}\right) \frac{\mathrm{Ra} - \mathrm{Ra}_t}{\mathrm{Ra}} \end{aligned} \tag{23}$$

where $\mathrm{Ra}_t = D_1 D_2 / B_1^2$. Hence, transition to the convective motion occurs at $r_t = 1.79$. This can be improved significantly in the case of (3, 2), in which case the additional modes $\mathbf{U}^{(016)}$, $\mathbf{U}^{(106)}$, $\Theta^{(013)}$, $\Theta^{(103)}$ are included in the representation of the flow in Eq. (21) and the transition occurs at $r_t = 1.009$. Even though the representation in Eq. (21) is not as accurate as in the case of (3, 2), we can still infer from Eq. (23) some qualitative properties of the flow as the convection sets in. The solution, Eq. (23), suggests that the rolls can be aligned along any horizontal direction, dictated only by the relative magnitudes of b_1, b_2 in $b_1^2 + b_2^2$ since $\mathbf{U}^{(011)}$ and $\mathbf{U}^{(101)}$ represent two-dimensional rolls aligned in the x and y directions, respectively. Orientational degeneracy of rolls appears in the linear theory of onset of convection [31]. A further well-known result follows from Eq. (23), that Ra_t is independent of Pr [20]. Since Nu is proportional to the heat flux at the boundary, it follows that

$$\mathrm{Nu} - 1 = -\left[\frac{d\overline{T}}{dz}\right]_{z=0} \propto c_0 \qquad \text{since} \quad \overline{T} = c_0 \Theta^{(001)} \tag{24}$$

where the overbar indicates averaging over the horizontal layer, and thus

$$\mathrm{Nu} - 1 \propto \frac{\mathrm{Ra} - \mathrm{Ra}_t}{\mathrm{Ra}} \tag{25}$$

which is known to hold in the case of stress-free boundary conditions ([31], p. 108).

While the stress-free case is used as the test database in this work due to its computational ease in direct numerical simulation and our objective being to develop and to demonstrate a robust K–L procedure, the present work can easily be extended to the physically more realistic case of no-slip boundary conditions. The robustness of the K–L basis in its present formulation together with its current implementation opens the way for further similar studies of transition in other phenomena.

REFERENCES

1. A. Schlüter, D. Lortz, and F. H. Busse, On the Stability of Steady Finite Amplitude Convection, *J. Fluid Mech.,* vol. 23, p. 129, 1965.
2. F. H. Busse, The Oscillatory Instability of Convection Rolls in a Low Prandtl Number Fluid, *J. Fluid Mech.,* vol. 52, pp. 97–112, 1972.
3. J. B. McLaughlin and S. A. Orszag, Transition from Periodic to Chaotic Thermal Convection, *J. Fluid Mech.,* vol. 122, pp. 123–142, 1982.
4. J. H. Curry, J. R. Herring, J. Loncaric, and S. A. Orszag, Order and Disorder in Two- and Three-Dimensional Benard Convection, *J. Fluid Mech.,* vol. 147, pp. 1–38, 1984.
5. D. Ruelle, F. Takens, and S. E. Newhouse, Occurence of Strange Axiom A Attractors Near Quasi Periodic Flows, *Commun. Math. Phys.,* vol. 64, pp. 35–40, 1978.
6. J. P. Gollub and S. V. Benson, Many Routes to Turbulent Convection, *J. Fluid Mech.,* vol. 100, pp. 449–470, 1980.
7. G. E. Willis and J. W. Deardorff, Development of Short-Period Temperature Fluctuations in Thermal Convection, *Phys. Fluids,* vol. 10, p. 931, 1967.
8. L. N. Howard, Convection at High Rayleigh Number, in *Proc. 11th Int. Congress of Applied Mechanics,* pp. 1109–1115, Springer-Verlag, Berlin, 1966.
9. R. Krishnamurti, On the Transition to Turbulent Convection. Part 1. The Transition from Two- to Three-Dimensional Flow, *J. Fluid Mech.,* vol. 42, pp. 295–307, 1970.
10. G. E. Willis and J. W. Deardorff, The Oscillatory Motions of Rayleigh Convection, *J. Fluid Mech.,* vol. 44, p. 661, 1970.
11. L. Sirovich and J. D. Rodriguez, Coherent Structures and Chaos: A Model Problem, *Phys. Lett. A*, vol. 120, pp. 211–214, 1987.
12. N. Aubry, P. Holmes, J. L. Lumley, and E. Stone, The Dynamics of Coherent Structures in the Wall Region of a Turbulent Boundary Layer, *J. Fluid Mech.,* vol. 192, p. 115, 1988.
13. X. Zhou and L. Sirovich, Coherence and Chaos in a Model of Turbulent Boundary Layer, *Phys. Fluids,* vol. 4, p. 12, 1992.
14. D. Rempfer and H. F. Fasel, Dynamics of Three-Dimensional Coherent Structures in a Flat Plate Boundary Layer, *J. Fluid Mech.,* vol. 275, p. 257, 1994.
15. H. Güneş, A. Liakopoulos, and R. A. Sahan, Low Dimensional Description of Oscillatory Thermal Convection: The Small Prandtl Number Limit, *Theor. Comput. Fluid Dynam.,* vol. 9, pp. 1–16, 1997.
16. L. Sirovich, M. Maxey, and I. H. Tarman, Analysis of Turbulent Thermal Convection, in J.-C. Andre, J. Cousteix, F. Durst, B. E. Launder, F. W. Schmidt and J. H. Whitelaw (eds.) *Turbulent Shear Flows,* 6 : Selected Papers from the Sixth International Symposium on Turbulent Shear Flows, Springer-Verlag, New York, pp. 68–77, 1987.
17. I. H. Tarman, A Karhunen–Loève Analysis of Turbulent Thermal Convection, *Int. J. Numer. Meth. Fluids,* vol. 22, pp. 67–79, 1996.
18. J. L. Lumley and A. Poje, Low-Dimensional Models for Flows with Density Fluctuations, *Phys. Fluids,* vol. 9, p. 7, 1997.
19. I. H. Tarman and L. Sirovich, Extensions to Karhunen–Loève Based Approximation of Complicated Phenomena, *Comput. Meth. Appl. Mech. Eng.,* vol. 155, pp. 359–368, 1998.
20. P. G. Drazin and W. H. Reid, *Hydrodynamic Stability,* Cambridge University Press, 1981.
21. C. Canuto, M. Hussaini, A. Quarteroni, and T. Zang, *Spectral Methods in Fluid Dynamics,* Springer-Verlag, New York, 1987.
22. J. L. Lumley, *Stochastic Tools in Turbulence,* Academic Press, New York, 1970.
23. L. Sirovich, Turbulence and the Dynamics of Coherent Structures, Parts 1–3, *Q. Appl. Math.,* vol. 45, p. 561, 1987.
24. G. Berkooz, P. Holmes, and J. L. Lumley, The Proper Orthogonal Decomposition in the Analysis of Turbulent Flows, *Annu. Rev. Fluid Mech.,* vol. 25, p. 539, 1993.

25. N. Aubry, W. Lian, and E. S. Titi, Preserving Symmetries in the Proper Orthogonal Decomposition, *SIAM J. Sci. Comput.,* vol. 14, no. 2, pp. 483–505, 1993.
26. I. H. Tarman, An Improved Dynamical Approximation to Boussinesq Equation Using Karhunen–Loève Basis, *Comput. Meth. Appl. Mech. Eng.,* vol. 144, pp. 153–162, 1997.
27. I. H. Tarman and L. Sirovich, A Parametric Study of Rayleigh–Benard Convection Using a Karhunen–Loève Basis, *11th Symp. on Turbulent Shear Flow,* Grenoble, France, 1997.
28. F. B. Lipps, Numerical Simulation of Three Dimensional Benard Convection in Air, *J. Fluid Mech.,* vol. 74, pp. 113–148, 1976.
29. R. M. Clever and F. H. Busse, Nonlinear Oscillatory Convection, *J. Fluid Mech.,* vol. 176, pp. 403–417, 1987.
30. A. E. Deane and L. Sirovich, A Computational Study of Rayleigh–Benard Convection, *J. Fluid Mech.,* vol. 222, pp. 231–250, 1991.
31. F. H. Busse, Transition to Turbulence in Rayleigh–Benard Convection, in H. L. Swinney and J. P. Gollub (eds.), *Hydrodynamic Instabilities and the Transition to Turbulence,* 2nd ed., Springer-Verlag, Berlin, 1985.